

Optimization strategies for operational parameters of Rydberg atom-based amplitude modulation receiver

Yuhao Wu(吴宇豪), Dongping Xiao(肖冬萍), Huaiqing Zhang(张淮清), and Sheng Yan(阎晟)

Citation: Chin. Phys. B, 2025, 34 (**1**): 013201. DOI: 10.1088/1674-1056/ad886a
Journal homepage: http://cpb.iphy.ac.cn; http://iopscience.iop.org/cpb

What follows is a list of articles you may be interested in

Optical storage of circular airy beam in atomic vapor

Hong Chang(常虹), Xin Yang(杨欣), Yan Ma(马燕), Xinqi Yang(杨鑫琪), Mingtao Cao(曹明涛), Xiaofei Zhang(张晓斐), Ruifang Dong(董瑞芳), and Shougang Zhang(张首刚)

Chin. Phys. B, 2024, 33 (**8**): 084202. DOI: 10.1088/1674-1056/ad4bbf

Optical PAM-4/PAM-8 generation via dual-Raman process in Rydberg atoms

Xiao-Yun Song(宋晓云), Zheng Yin(尹政), Guan-Yu Ren(任冠宇), Ming-Zhi Han(韩明志), Ai-Hong Yang(杨艾红), Yi-Hong Qi(祁义红), and Yan-Dong Peng(彭延东)

Chin. Phys. B, 2024, 33 (**6**): 064203. DOI: 10.1088/1674-1056/ad3344

Extending microwave-frequency electric-field detection through single transmission peak method

ing Liu(刘青), Jin-Zhan Chen(陈进湛), He Wang(王赫), Jie Zhang(张杰), Wei-Min Ruan(阮伟民), Guo-Zhu Wu(伍国柱), Shun-Yuan Zheng(郑顺元), Jing-Ting Luo(罗景庭), and Zhen-Fei Song(宋振飞)

Chin. Phys. B, 2024, 33 (**5**): 054203. DOI: 10.1088/1674-1056/ad2a6f

Effectively modulating spatial vortex four-wave mixing in a diamond atomic system

Nuo Ba(巴诺), Ming-Qi Jiang(姜明奇), Jin-You Fei(费金友), Dan Wang(王丹), Hai-Lin Jiang(蒋海林), Lei Wang(王磊), and Hai-Hua Wang(王海华)

Chin. Phys. B, 2024, 33 (**4**): 044202. DOI: 10.1088/1674-1056/ad0771

Numerical studies of atomic three-step photoionization processes with non-monochromatic laser fields

Xiao-Yong Lu(卢肖勇), Li-De Wang(王立德), and Yun-Fei Li(李云飞)

Chin. Phys. B, 2022, 31 (**6**): 063203. DOI: 10.1088/1674-1056/ac490b

---

Optimization strategies for operational parameters of Rydberg atom-based amplitude modulation receiver

Yuhao Wu(吴宇豪), Dongping Xiao(肖冬萍)†, Huaiqing Zhang(张淮清), and Sheng Yan(阎晟)

National Key Laboratory of Power Transmission Equipment Technology, School of Electrical Engineering, Chongqing University, Chongqing 40044, *China*

(Received 13 July 2024; revised manuscript received 21 September 2024; accepted manuscript online 18 October 2024)

The Rydberg atom-based receiver, as a novel type of antenna, demonstrates broad application prospects in the field of microwave communications. However, since Rydberg atomic receivers are nonlinear systems, mismatches between the parameters of the received amplitude modulation (AM) signals and the system's linear workspace and demodulation operating points can cause severe distortion in the demodulated signals. To address this, the article proposes a method for determining the operational parameters based on the mean square error (MSE) and total harmonic distortion (THD) assessments and presents strategies for optimizing the system's operational parameters focusing on linear response characteristics (LRC) and linear dynamic range (LDR). Specifically, we employ a method that minimizes the MSE to define the system's linear workspace, thereby ensuring the system has a good LRC while maximizing the LDR. To ensure that the signal always operates within the linear workspace, an appropriate carrier amplitude is set as the demodulation operating point. By calculating the THD at different operating points, the LRC performance within different regions of the linear workspace is evaluated, and corresponding optimization strategies based on the range of signal strengths are proposed. Moreover, to more accurately restore the baseband signal, we establish a mapping relationship between the carrier Rabi frequency and the transmitted power of the probe light, and optimize the slope of the linear demodulation function to reduce the MSE to less than 0.8×10^{-4}. Finally, based on these methods for determining the operational parameters, we explore the effects of different laser Rabi frequencies on the system performance, and provide optimization recommendations. This research provides robust support for the design of high-performance Rydberg atom-based AM receivers.

Keywords: Rydberg atom-based receiver, amplitude modulation (AM), operating parameters, optimization

PACS: 32.80.Ee, 42.50.Gy, 42.60.Fc, 84.30.Qi

DOI: 10.1088/1674-1056/ad886a **CSTR:** 32038.14.CPB.ad886a

1. Introduction

Rydberg atom-based receivers are used in electric field measurements due to their large polarizability and microwave-transition dipole moments.[1] These sensors offer self-calibration,[2,3] high sensitivity,[4] and broad operating frequency,[5,6] making them superior to traditional RF and microwave technologies. By utilizing phenomena such as electromagnetically induced transparency (EIT) and the Autler–Townes (AT) effect, Rydberg sensors can measure electric fields from DC to THz frequencies. This capability enables the precise measurements of field strength,[7–11] polarization,[12,13] and phase.[14–16] Innovative technologies, including atomic superheterodyne receivers,[17] the use of cold atoms,[18,19] and microwave resonators,[20] have further enhanced the sensors' sensitivity and resolution. Over the past decade, these advancements have significantly expanded the capabilities of Rydberg quantum sensors, enabling their applications in communication,[21] imaging,[22,23] and metrology.[3]

Compared to traditional electronic receivers, Rydberg atom-based receivers exhibit higher sensitivity, particularly suited for long-distance and weak signals.[24] These receivers benefit from quantum projection noise, which is much smaller than thermal noise, and a higher signal-to-noise ratio that enhances data transfer capabilities.[25–27] Recent research has shown that Rydberg atomic-based sensors can detect multiple modulation signals, including[28–31] amplitude modulation (AM), frequency modulation (FM), and phase modulation (PM). Current research has made progress in enhancing the sensitivity,[32,33] linear dynamic range,[27] anti-jamming capabilities, data transmission capacity,[34,35] as well as multi-band and multi-channel transmission[24,36] of receivers.

However, these studies do not mention the impact of Rydberg atomic receiver operational parameters on system performance. For AM signals, the direct real-time readout feature of the Rydberg atomic AM receiver depends on the approximate linear relationship between the carrier amplitude and the power of the resonant probe light transmission. However this approximately linear relationship only exists within a smaller interval of the nonlinear relationship, known as the linear workspace. The linear dynamic range (LDR) and linear response characteristics (LRC) within the linear workspace are crucial performance metrics. LDR refers to the range of signal strengths that the system can receive without distortion. LRC refers to the linearity within the linear workspace; a good LRC helps prevent excessive mixing of higher harmonics that could

†Corresponding author. E-mail: xiaodongping@cqu.edu.cn

© 2025 Chinese Physical Society and IOP Publishing Ltd. All rights, including for text and data mining, AI training, and similar technologies, are reserved.

overlap with the baseband signal spectrum. Exceeding the LDR or operating in a region with poor LRC will lead to signal distortion, as observed in Refs. [21,26]. Moreover, the slope of the linear workspace directly affects the baseband signal gain. Reference [32] explores the LDR and baseband signal gain of Rydberg atom receivers, but the analysis of how operating parameters affect these performance metrics is not comprehensive enough, and the conclusions lack support from some experimental data. Furthermore, to ensure that the baseband signal operates only within the linear workspace, an appropriate demodulation operating point must be set. Reference [37] emphasizes the importance of choosing a demodulation operating point and proposes a simple model, but lacks a detailed discussion on how to optimize this choice considering both the LDR and LRC, and its operability is poor. Therefore, understanding the mechanisms by which operating parameters affect system performance and proposing optimization strategies to meet different needs are crucial for the design and application of Rydberg atom receivers.

This work explores optimization strategies for Rydberg atom receivers processing AM signals using room-temperature Cs atoms. By tuning the frequencies of the coupling light, probe light, and carrier signal to resonate with Rydberg atom energy levels, we measured the probe light's resonant transmission power at various carrier Rabi frequencies. Based on this, we developed an optimization method using the mean square error (MSE) to balance LDR and LRC within the linear workspace. Further improvements were achieved by optimizing the slope of the linear demodulation function, significantly reducing MSE. Total harmonic distortion (THD) was calculated to evaluate the impact of different demodulation points on LRC, providing strategies for selecting optimal operating points. We also analyzed the effects of baseband signal gain on system sensitivity and examined how LDR and gain vary with different Rabi frequencies, guiding the choice of laser parameters. These strategies, though demonstrated with AM modulation, are adaptable to other analog and digital schemes, aiding the design of Rydberg atom microwave sensors and related protocols.

2. Principles and methods

This section introduces the theoretical model and working principles of the Rydberg atom-based AM receiver.

2.1. Theoretical model

The atomic energy level diagram relevant to this study is depicted in Fig. 1(a). A weak probe field drives atoms from the ground state $6S_{1/2}$ to the intermediate state $6P_{3/2}$, while a strong coupling field excites them from the intermediate state to the Rydberg state $nD_{5/2}$. Rydberg states, characterized by high principal quantum numbers (n), are highly sensitive to external electric fields. The applied resonant microwave electric field induces a transition in the Rydberg state from $nD_{5/2}$ to $(n+1)P_{3/2}$, causing the EIT peak to split into two due to the AT effect, as depicted in Fig. 1(b).

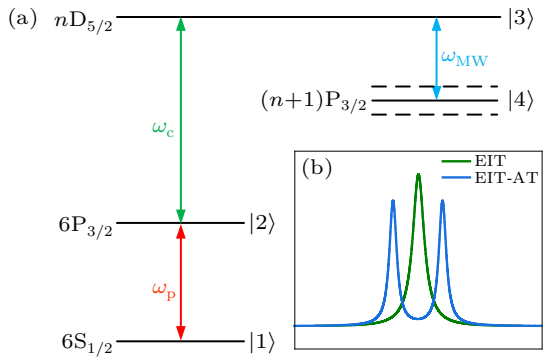


Fig. 1. (a) Schematic diagram of the four-level system of Cs atoms. (b) Schematic diagram of EIT-AT splitting.

The interval (Δ_{AT}) between these split peaks is linearly related to the strength of the resonant microwave electric field (E_{MW})[7]

$$\Delta_{AT} = \Omega_{MW} = \frac{\mu_{MW}}{\hbar} E_{MW}, \tag{1}$$

where $\hbar$ represents the reduced Planck constant; μ_{MW} is the transition dipole moment of the microwave field; Ω_{MW} is the Rabi frequency of the microwave field.

Microwave AM fields consist of two components: the baseband signal, $E_{Sig}(t)$, and the carrier wave, $E_{MW}(t)$. The carrier frequency matches the resonance frequency of the microwave field. The AM field can be represented as

$$\begin{aligned} E_{AM}(t) &= (1+E_{Sig}(t))E_{MW}(t) \\ &= (1+k\cos(\omega_{Sig}t))E_{MW}\cos(\omega_{MW}t), \end{aligned} \tag{2}$$

where $k = E_{Sig}/E_{MW}$ represents the modulation depth, it is crucial to ensure $k < 1$ during the amplitude modulation process to avoid signal distortion; ω is the angular frequency. The baseband signal frequency usually falls within the hundreds of kHz or lower, whereas the Rydberg energy level resonance frequency exceeds GHz, thus $\omega_{Sig} \ll \omega_{MW}$.

We incorporate the Hamiltonian of the AM field interacting with atoms into the EIT three-level system. Using the rotating wave approximation, the total Hamiltonian of the system in matrix form is

$$H = \frac{\hbar}{2}\begin{pmatrix} 0 & \Omega_p & 0 & 0 \\ \Omega_p & -2\Delta_p & \Omega_c & 0 \\ 0 & \Omega_c & -2(\Delta_p+\Delta_c) & \Omega_{MW}+\frac{1}{2}(e^{-i\omega_{Sig}t}+e^{i\omega_{Sig}t})\Omega_{Sig} \\ 0 & 0 & \Omega_{MW}+\frac{1}{2}(e^{i\omega_{Sig}t}+e^{-i\omega_{Sig}t})\Omega_{Sig} & -2(\Delta_p+\Delta_c-\Delta_{MW}) \end{pmatrix}, \tag{3}$$

where Δ_p, Δ_c, and Δ_{MW} represent the detuning of the probe light, coupling light, and resonant microwave field respectively; Ω_p and Ω_c denote the Rabi frequencies of the probe light and coupling light.

In the thermal atomic system, the Lindblad master equation (Eq. (4)) is used to describe the dynamics of atomic decay. To account for the Doppler effect, we modify the thermal atomic density matrix (Eq. (5)).[6,17]

$$\dot{\rho} = \frac{\mathrm{d}\rho}{\mathrm{d}t} = -\frac{\mathrm{i}}{\hbar}[H,\rho] + L(\rho), \tag{4}$$

$$\rho_{21_D} = \frac{1}{\sqrt{\pi}u}\int_{-3u}^{3u} \rho_{21}(\Delta_p', \Delta_c')\, \mathrm{e}^{\frac{-v^2}{u^2}}\, \mathrm{d}v, \tag{5}$$

where $L(\rho)$ represents the Lindblad operator that explains the atomic decay process; ρ_{21} is the detected optical raw density matrix element obtained by solving the Bloch equation; $\Delta'_{p(c)} = \Delta_{p(c)} \pm 2\pi v/\lambda_{p(c)}$ is the probe (coupling) light detuning corrections; $u = (2k_B T/m)^{1/2}$, m is the atom's mass, k_B is Boltzmann constant, and T is the thermodynamic temperature.

We then calculated the complex polarizability χ of the probe light

$$\chi = \frac{2N_0\mu_p^2}{\varepsilon_0\hbar\Omega_p}\rho_{21_D}, \tag{6}$$

where N_0 is the total atomic number density; μ_p is the transition dipole moment of the probe light; ε_0 is the vacuum dielectric constant.

According to the Beer–Lambert Law, the transmission power of the probe light is given by[32]

$$I = I_0 \exp\left(-k_p L \mathrm{Im}[\chi]\right), \tag{7}$$

where I_0 is the incident probe light power; $k_p = 2\pi/\lambda_p$ is the wave number of the probe light; and L is the propagation distance of the probe light in the atomic vapor.

At this point, the probe light, coupling light, and microwave field are in resonance with the atomic energy levels, i.e., $\Delta_p = 0$, $\Delta_c = 0$, and $\Delta_{MW} = 0$. Using the aforementioned formula, one can calculate the resonant transmission power of the probe light in the thermal atomic system.

2.2. Demodulation principles

The AM signal consists of the baseband signal carrying the information and the carrier signal aiding transmission. Demodulation denotes the extraction of the original baseband signal from the received modulated signal. Traditional methods include envelope and synchronous detection. Rydberg atoms, however, exhibit inherent demodulation capabilities. When exposed to an AM field, Rydberg atoms absorb the carrier signal, causing the EIT spectrum to show AT splitting or the AC Stark effect. This allows direct retrieval of the baseband signal through variations in the EIT spectrum. Unlike traditional methods, Rydberg atom sensors do not require additional coherent signals or demodulation circuits.

When the coupling light, probe light, and carrier signal resonate with the Rydberg atom energy levels, the probe light transmission power shows a nonlinear relationship with the carrier signal amplitude. Within this curve exists a nearly linear section, the linear workspace, where changes in carrier amplitude correspond directly to changes in probe light transmission power. Monitoring this power allows direct demodulation of the baseband signal.

Figure 2 elucidates the demodulation principle of the Rydberg atomic AM signal reception system. Initially, it is essential to establish the probe light's resonant transmission power curve (Fig. 2, blue curve), calculated under resonant conditions according to Eq. (7). The region marked in red (Fig. 2, red line) delineates the linear workspace. Subsequently, setting a bias operating point (Fig. 2, black dot) is crucial to ensure that the introduction of an AM signal remains confined within this linear domain. Upon reception, the carrier Rabi frequency (Fig. 2, green curve) contains information from the baseband signal. By combining Eqs. (1) and (2), the expression for the carrier Rabi frequency is given as follows:

$$\begin{aligned}\Omega_{MW}(t) &= \Omega_{op} + \Omega_{Sig}(t)\\ &= \Omega_{op} + \Omega_{Sig}\cos(\omega_{Sig}t)\\ &= \Omega_{op}(1 + k\cos(\omega_{Sig}t)),\end{aligned} \tag{8}$$

where $\Omega_{Sig}(t)$ is the Rabi frequency form of the baseband signal; and k is the modulation depth, which better represents the relative size of the baseband signal to the operating point amplitude.

Within the linear workspace, the mapping relationship between the probe light's resonance transmission power and the Rabi frequency is established by the demodulation linear function $g(x) = \kappa x + g(0)$ (Fig. 2, red line). The Rydberg atomic reception system processes and demodulates this signal, producing a resonant transmission signal (Fig. 2, orange curve) through a mapping relationship within this workspace.

$$I_{Sig}(t) = g(\Omega_{MW}(t)) = \beta\Omega_{op} + \kappa\Omega_{Sig}(t), \tag{9}$$

where $\beta\Omega_{op}$ is a constant determined by the operating point, which can specifically be written as $\beta\Omega_{op} = \kappa\Omega_{op} + g(0)$; $\kappa = \mathrm{d}g(x)/\mathrm{d}x$.

With this, we can calculate the original baseband signal through the resonant transmission signal $I_{Sig}(t)$ of the probe light,

$$E_{Sig}(t) = \frac{\hbar\Omega_{Sig}(t)}{\mu_{MW}} = \frac{\hbar(g^{-1}(I_{Sig}(t)) - \Omega_{op})}{\mu_{MW}}. \tag{10}$$

In practical applications, the Rydberg atom demodulation system will also include modules for filtering and noise reduction. The description provided here just outlines the basic principle of Rydberg atom demodulation.

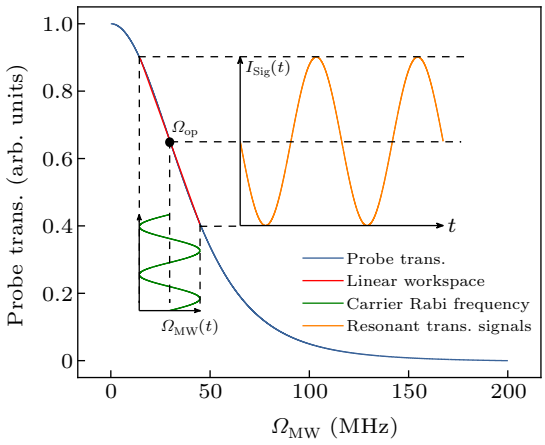


Fig. 2. Schematic diagram of the working principle of AM signal demodulation. The blue curve represents the probe light resonant transmission power I varying with the carrier amplitude $\Omega_{\rm MW}$. The red line indicates the linear workspace, described by the demodulation linear function $g(x)$. The green curve shows the temporal variation of the carrier Rabi frequency $\Omega_{\rm MW}(t)$, while the orange curve depicts the resonant transmission signal $I_{\rm Sig}(t)$.

3. Experimental setup

The Rydberg atom preparation system and the signal loading/receiving device are depicted in Fig. 3(a). The experiment employs a weak probe laser (852 nm, $\Omega_{\rm p} = 2\pi \times$ 8.91 MHz) and a strong coupling laser (509 nm, $\Omega_{\rm c} = 2\pi \times$ 17.24 MHz). This setup excites the atoms in the chamber to Rydberg states. The atoms chamber measures 50 mm in length. Firstly, by utilizing the frequency stabilization method of saturated absorption spectroscopy, the probe light and coupling light are precisely locked to the resonance transition frequencies of the $|6S_{1/2}, F = 4\rangle \rightarrow |6P_{3/2}, F' = 5\rangle$ and $|6P_{3/2}, F' = 5\rangle \rightarrow 50D_{5/2}$ energy levels, respectively. When the frequency of the coupling light is scanned, a photodetector captures the transmitted light passing through the atom vapor, facilitating the acquisition of the EIT spectrum. A microwave electric field at a frequency of 5.702 GHz is applied to the atomic atoms vapor using a horn antenna. This frequency is near the transition frequency between the $50D_{5/2} \rightarrow 51P_{3/2}$ Rydberg energy levels. By aligning the polarization direction of the microwave field with that of the lasers, a four-level Rydberg atom system is established under the microwave field, resulting in a stable AT splitting in the EIT spectrum (Fig. 3(b)). The microwave AM field is achieved using an external mixer, which allows for the independent adjustment of the frequency and amplitude of both the carrier signal and the baseband signal.

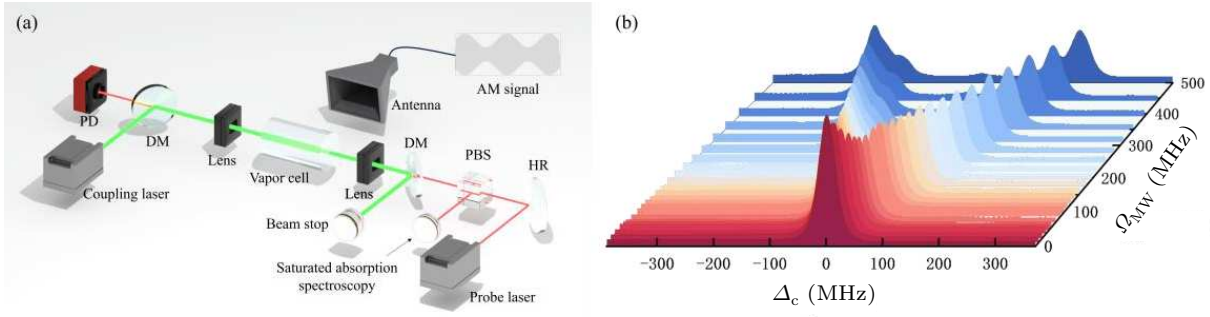


Fig. 3. (a) Schematic of the experimental setup. (b) Experimental data chart of splitting under different Rabi frequency carriers.

4. Results and discussion

This section comprehensively evaluates system performance, including linear response characteristics, linear dynamic range, and baseband signal gain. The linear operating region is determined using mean square error (MSE) calculations. The effects of demodulation operating points, linear demodulation functions, and laser Rabi frequencies on system performance are analyzed. Based on these analyses, optimization strategies for operating parameters are proposed.

4.1. Linear workspace

The LRC of the linear workspace is crucial for maintaining baseband signal fidelity, which typically spans a specific bandwidth range. Poor LRC can result in higher harmonics overlapping with the baseband signal, complicating their elimination with filtering modules. Additionally, the LDR dictates the allowable baseband signal intensity range; exceeding this range leads to severe signal distortion. For a fixed Rydberg atom receiver with defined energy levels and laser Rabi frequency, LRC and LDR are inherently conflicting parameters. Expanding the LDR tends to impair the LRC. Therefore, balancing these two parameters to determine the optimal linear workspace is necessary.

Before this, we need to obtain the resonant transmission power curve of the probe light. In the experiment, the frequencies of the coupling light, probe light, and carrier signal are locked to the resonance frequencies of the Rydberg atom energy levels. By varying the amplitude of the carrier signal and recording the transmission power ($n = 5$), we obtain the data shown in Fig. 4(a). The red curve represents the theoretical calculation, and all data is normalized. To determine the linear workspace, we first derive the demodulation linear function for the workspace (Fig. 4(b) red line). This line represents the tangent equation at the inflection point of the probe light's

resonant transmission power curve, which can be expressed as

$$g(x) = \kappa(x - \Omega_0) + I(\Omega_0), \tag{11}$$

where Ω_0 is obtained by solving for $\partial^2 I/\partial\Omega_{\mathrm{MW}}^2 = 0$. We use the MSE to determine the degree of overlap between the resonant transmission power curve of the probe light and the demodulation linear function. A smaller MSE indicates a higher degree of overlap, meaning better LRC. The MSE is calculated using the formula

$$\mathrm{MSE} = \frac{1}{n}\sum_{i=1}^{n}(I_i - g_i)^2, \tag{12}$$

where n is the number of samples. The MSE calculation results are shown by the blue line in Fig. 4(b). The yellow area represents the range where MSE $< 10^{-3}$, indicating good LRC.

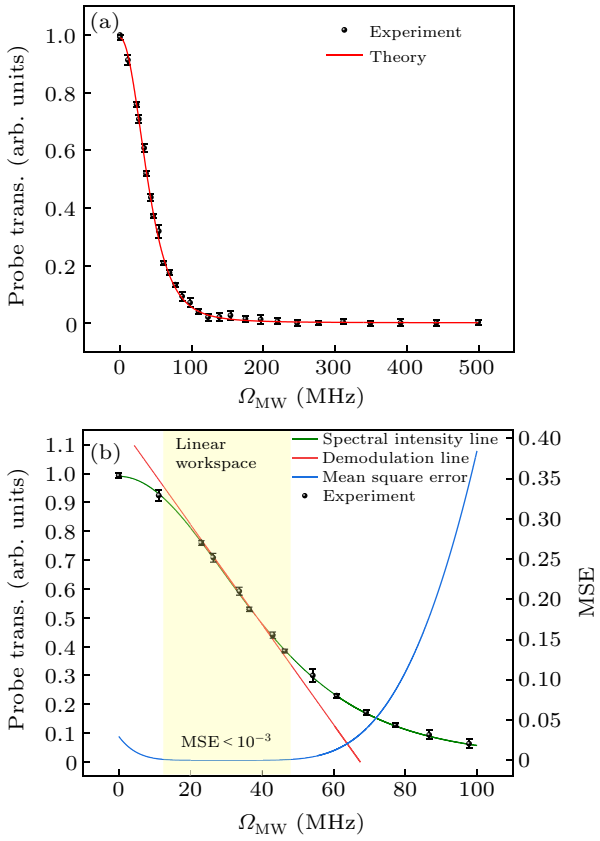


Fig. 4. (a) Experimental data and theoretical calculation results of the probe light's resonant transmission power. (b) Schematic diagram of the method for determining the linear workspace. The green line represents the probe light's resonant transmission power curve, the red line represents the demodulation linear function used to determine the linear workspace, and the blue line represents the MSE between the two.

The resulting linear workspace is [12.4412, 47.9848] MHz. If the inflection point (Ω_{op} = 28.9224 MHz) is chosen as the operation point, the LDR of the system is [12.4412, 45.4036] MHz, with a modulation depth not exceeding 56.98%. In the experiment, the operating point is set at the inflection point, and the baseband signal is a 1 kHz cosine signal with modulation depths of 10%, 50%, and 70%. The $I_{\mathrm{Sig}}(t)$ after filtering out the DC component is shown in Fig. 5. The gray points represent experimental data, while the other colors represent fitted curves. To make the experimental phenomena more apparent and to account for noise, some margin is left. Within the LDR, the baseband signal maintains good fidelity, while outside this range, severe nonlinear distortion occurs. Thus, this method, which uses MSE to determine the linear workspace, is more stable and faster compared to Ref. [29]. It ensures good fidelity while maximizing the LDR.

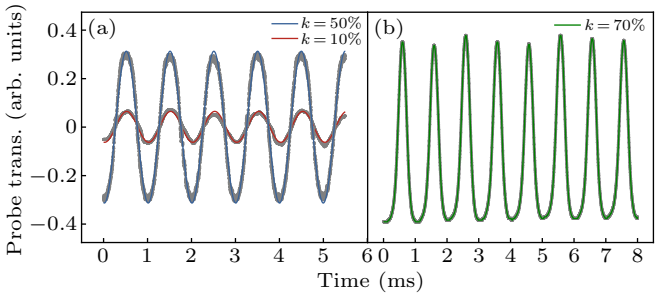


Fig. 5. Received resonant transmission signals $I_{\mathrm{Sig}}(t)$ at different baseband signal strengths. The gray points represent experimental data, while the other colors represent fitted curves. (a) Signal strength within the LDR, with modulation depths of 10% (red line) and 50% (blue line). (b) Signal strength outside the LDR, with a modulation depth of 70% (green line).

4.2. Demodulation operating point

When processed by a nonlinear system like the Rydberg atom-based receiver, a signal not only retains its fundamental frequency component but also generates various harmonic components — integer multiples of the fundamental frequency. These harmonics introduce distortions, causing the output signal to diverge from the input signal. Since the linear workspace is inherently nonlinear, different regions have different LRC. Areas with poorer LRC will introduce more unnecessary harmonic components. This raises the question of which part of the linear workspace the baseband signal should operate within, which is essentially the issue of selecting the demodulation operating point.

Total harmonic distortion (THD) is an indicator used to measure the extent of distortion in a signal due to harmonic components. Therefore, THD can be used to evaluate which region of the linear workspace introduces fewer harmonic components, resulting in a better LRC. This helps optimize the selection of the demodulation operating point. THD is defined as

$$\mathrm{THD} = 20\log_{10}\left(\frac{\sqrt{V_2^2 + V_3^2 + V_4^2 + \cdots + V_n^2}}{V_1}\right), \tag{13}$$

where V_1 represents the amplitude of the fundamental frequency; $V_2, V_3, V_4, \ldots, V_n$ represents the amplitudes of the various harmonic frequencies.

We calculated the THD for the first 10 harmonics at different demodulation operating points for three sets of baseband signal strengths (Ω_{Sig} = 2.89 MHz, 5.78 MHz, 8.67 MHz), as shown in Fig. 6(a). Clearly, as the operating

point shifts, the THD for all three data sets reaches its minimum at the inflection point of the probe light's resonant transmission power curve. This indicates that the area near the inflection point offers the best LRC. This suggests that setting the operating point near the curve's inflection point optimizes the system's performance by minimizing harmonic distortions. Figure 6(b) displays the THD ($n = 10$) for different baseband signal strengths with the demodulation operating point set at both the midpoint (the midpoint of the LDR) and the inflection point. Within the LDR, the LRC when the operating point is set at the inflection point consistently outperforms those at the midpoint, achieving a THD of less than -90 dB for very low baseband signal strengths. However, we should not hastily conclude that the inflection point is the optimal demodulation operating point.

Considering the LDR, choosing the midpoint ($\Omega_{\rm op} = 30.213$ MHz) as the demodulation operating point allows the LDR to cover the entire linear workspace with the maximum modulation depth increased to 58.82%. Unlike Ref. [37], which only considers the LRC at the inflection point, we have systematically analyzed the impact of different demodulation operating points on the LRC from the perspective of THD. Additionally, we offer an optimization strategy that allows for flexible selection of operating points based on the strength of the baseband signal.

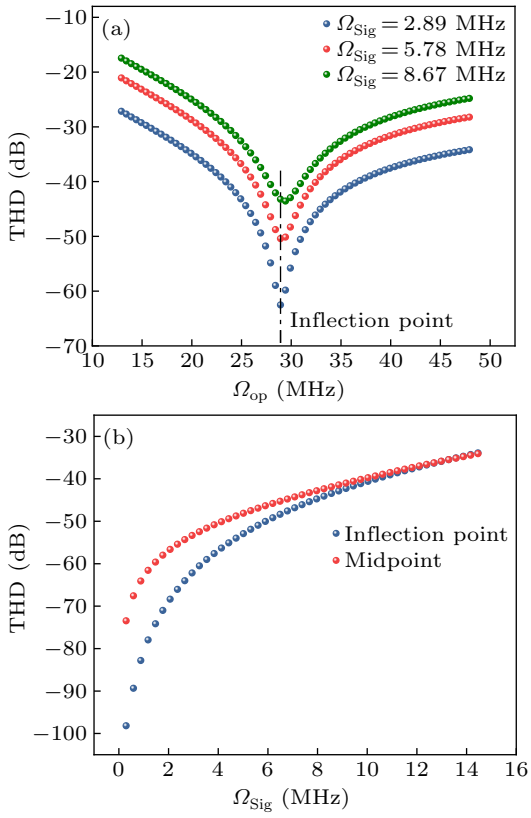


Fig. 6. THD calculation results. (a) THD at different demodulation operating points for baseband signal strengths at 2.89 MHz (blue points), 5.78 MHz (red points), and 8.67 MHz (green points). (b) THD for different baseband signal strengths when the demodulation operating point is set at the inflection point (red points) and the midpoint (blue points).

4.3. Demodulation linear function

After obtaining the resonant transmission signal of the probe light, it is crucial to input this data into Eq. (10) to retrieve the original baseband signal. Acquiring an accurate demodulation linear function (Eq. (11)) is essential for this process. In Subsection 3.1, to explore the method for determining the linear workspace, we selected the tangent equation at the inflection point of the probe light's resonant transmission power curve as the demodulation linear function $g(x)$. However, this approach is not entirely accurate for signal demodulation. The tangent equation shows that on the left side of the inflection point, $\partial^2 I/\partial\Omega_{\rm MW}^2 < 0$, while on the right side, $\partial^2 I/\partial\Omega_{\rm MW}^2 > 0$. This indicates that the curve gradually deviates from the tangent equation on both sides (as illustrated by the red and green lines in Fig. 4(b)). Using this tangent equation as the demodulation linear function could result in an underestimation of the baseband signal strength $E_{\rm Sig}(t)$. Therefore, it is advisable to optimize the demodulation linear function during the demodulation process to ensure more accurate retrieval of the original baseband signal.

Based on the analysis in Subsection 3.2, the area around the inflection point of the probe light's resonant transmission power curve offers the best LRC. Therefore, we focus on optimizing the slope κ of the demodulation linear function. By passing the linear function through the inflection point and gradually increasing the slope, we compute the MSE within the linear workspace, as shown in Fig. 7. Here, $\kappa = -0.01733$ represents the slope of the tangent equation (black line). When $\kappa = -0.01583$ (blue line), the MSE between the probe light's resonant transmission power curve and the demodulation linear function is less than 0.8×10^{-4}, which is an improvement of more than an order of magnitude compared to the black line. At this point, the demodulation linear function more accurately fits within the linear workspace, providing a more precise framework for demodulating the signal.

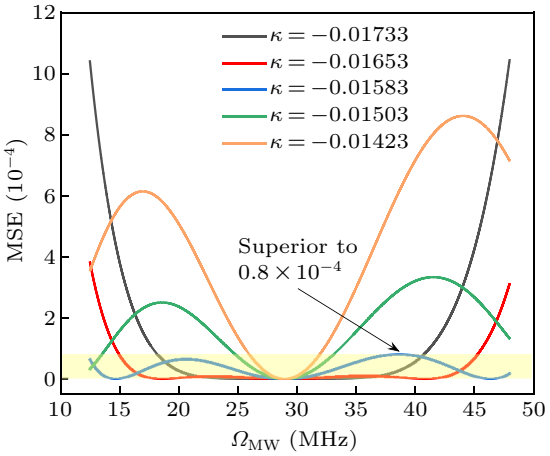


Fig. 7. Calculating the MSE for demodulation linear function slopes from -0.01733 to -0.01423 and achieving minimum MSE within LDR at $\kappa = -0.01583$ (blue line), and MSE $< 0.8 \times 10^{-4}$ (light yellow area).

4.4. Laser Rabi frequency

After filtering out the DC component in Eq. (9), it can be rewritten as $|\kappa| = \left|I_{\mathrm{Sig}}(t)/\Omega_{\mathrm{Sig}}(t)\right|$, so $|\kappa|$ can be referred to as the baseband signal gain. As $|\kappa|$ increases, the intensity of the baseband signal in the resonant transmission power of the probe light is amplified. This effectively suppresses the electronic noise present in subsequent signal processing, thereby enhancing system sensitivity. However, as $|\kappa|$ increases, the projection range of the linear workspace on Ω_{MW} decreases, indicating a compression of the LDR. For a fixed atomic receiving system (as discussed in Section 2), $|\kappa|$ is fixed. Therefore, we explore the impact of changing the laser Rabi frequency on $|\kappa|$ and the LDR. Due to the changes in the laser Rabi frequency causing variations in EIT spectrum intensity, we have normalized the results.

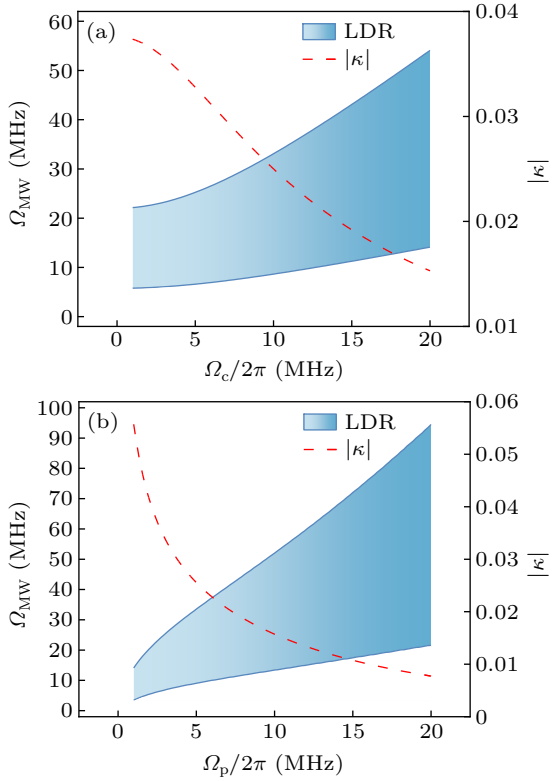


Fig. 8. LDR (blue area) and baseband signal gain (red dashed line) under different laser Rabi frequencies. (a) Coupling light Rabi frequency. (b) Probe light Rabi frequency.

Figure 8 displays the variation of $|\kappa|$ and LDR under different coupling light (Fig. 8(a)) and probe light (Fig. 8(b)) Rabi frequencies. It can be observed that as the Rabi frequencies of the coupling or probe light increase, $|\kappa|$ gradually decreases while the LDR continuously increases, which is consistent with our analysis. Although $|\kappa|$ and LDR exhibit similar trends, the extents of changes induced by the Rabi frequencies of the coupling light or probe light are different. When Ω_{p} (probe light Rabi frequency) is weaker, $|\kappa|$ rapidly declines, indicating that a weaker Ω_{p} has a significant impact on system sensitivity; therefore, it is advisable to reduce Ω_{p} appropriately. However, at this time, the system's LDR is very small (as shown in Fig. 8(b)), and since the decline of $|\kappa|$ in Fig. 8(a) is more gradual, increasing Ω_{c} (coupling light Rabi frequency) has a lesser impact on system sensitivity, and thus Ω_{c} can be appropriately increased to enlarge the LDR.

In summary, the effects of Ω_{c} and Ω_{p} on the performance of the Rydberg atom receiver are complex and require a comprehensive consideration based on the actual situation to select suitable parameters.

5. Conclusion

Overall, this paper investigates how the operating parameters of Rydberg atom AM receivers affect the linear dynamic range (LDR), linear response characteristics (LRC), and baseband signal gain, and proposes corresponding optimization strategies. Firstly, we calculate the mean square error (MSE) between the resonant transmission power curve of the probe light and the tangent equation at its inflection point, identifying regions where MSE $< 10^{-3}$ in the linear workspace. Experiments show that within this linear workspace, the baseband signal maintains good fidelity, while severe signal distortion occurs outside this region, validating our method for determining the linear workspace. We then investigate the selection of the demodulation operating point within the linear operating region, comparing the inflection point of the resonant transmission power curve of the probe light with the midpoint of the linear operating region. Using total harmonic distortion (THD) to evaluate LRC performance, the results indicate that the inflection point as the demodulation operating point offers the best LRC, with THD reaching -90 dB or higher for weaker baseband signals. Conversely, the midpoint of the linear workspace as the demodulation operating point provides the best LDR, covering the entire linear workspace. To obtain a more accurate original baseband signal, we optimized the slope of the linear demodulation function. This optimization resulted in an MSE $< 0.8 \times 10^{-4}$ between the linear demodulation function and the actual resonant transmission power curve of the probe light, improving the MSE metric by an order of magnitude. Finally, we analyzed the relationship between baseband signal gain and system sensitivity. Based on the influence of the laser Rabi frequency on LDR and baseband signal gain, we propose recommendations for selecting the laser Rabi frequency in the Rydberg atom AM receiving system.

Although AM technology is the most fundamental modulation mode, it is also the most representative in the demodulation process of Rydberg atom receivers. The parameter optimization strategies studied in this paper can be extended to other modulation modes, including phase modulation and digital amplitude modulation signals. This research is expected to promote the design of Rydberg atom microwave sensors and the development of related operating protocols.

Acknowledgments

Project supported by the National Natural Science Foundation of China (Grant No. U22B2095) and the Civil Aerospace Technology Research Project (Grant No. D010103).

References

[1] Gallagher T F 1988 *Rep. Prog. Phys.* **51** 143
[2] Anderson D A, Miller S A, Raithel G, Gordon J A, Butler M L and Holloway C L 2016 *Phys. Rev. Appl.* **5** 034003
[3] Holloway C L, Gordon J A, Jefferts S, Schwarzkopf A, Anderson D A, Miller S A, Thaicharoen N and Raithel G 2014 *IEEE Trans. Antennas Propag.* **62** 6169
[4] Fan H, Kumar S, Sedlacek J, Kuebler H, Karimkashi S and Shaffer J P 2015 *J. Phys. B-At. Mol. Opt. Phys.* **48** 202001
[5] Simons M T, Gordon J A and Holloway C L 2016 *J. Appl. Phys.* **120** 123103
[6] Holloway C L, Simons M T, Gordon J A, Dienstfrey A, Anderson D A and Raithel G 2017 *J. Appl. Phys.* **121** 233106
[7] Sedlacek J A, Schwettmann A, Kuebler H, Loew R, Pfau T and Shaffer J P 2012 *Nat. Phys.* **8** 819
[8] Bason M G, Tanasittikosol M, Sargsyan A, Mohapatra A K, Sarkisyan D, Potvliege R M and Adams C S 2010 *New J. Phys.* **12** 065015
[9] Jiao Y, Han X, Yang Z, Li J, Raithel G, Zhao J and Jia S 2016 *Phys. Rev. A* **94** 023832
[10] Paradis E, Raithel G and Anderson D A 2019 *Phys. Rev. A* **100** 013420
[11] Gordon J A, Holloway C L, Schwarzkopf A, Anderson D A, Miller S, Thaicharoen N and Raithel G 2014 *Appl. Phys. Lett.* **105** 024104
[12] Sedlacek J A, Schwettmann A, Kuebler H and Shaffer J P 2013 *Phys. Rev. Lett.* **111** 063001
[13] Jiao Y, Hao L, Han X, Bai S, Raithel G, Zhao J and Jia S 2017 *Phys. Rev. Appl.* **8** 014028
[14] Simons M T, Haddab A H, Gordon J A and Holloway C L 2019 *Appl. Phys. Lett.* **114** 114101
[15] Anderson D A, Sapiro R E, Goncalves L F, Cardman R and Raithel G 2022 *Phys. Rev. Appl.* **17** 044020
[16] Liu X B, Jia F D, Zhang H Y, Mei J, Liang W C, Zhou F, Yu Y H, Liu Y, Zhang J, Xie F and Zhong Z P 2022 *Chin. Phys. B* **31** 090703
[17] Jing M, Hu Y, Ma J, Zhang H, Zhang L, Xiao L and Jia S 2020 *Nat. Phys.* **16** 911
[18] Liao K Y, Tu H T, Yang S Z, Chen C J, Liu X H, Liang J, Zhang X D, Yan H and Zhu S L 2020 *Phys. Rev. A* **101** 053432
[19] Zhou F, Jia F, Liu X, Yu Y, Mei J, Zhang J, Xie F and Zhong Z 2023 *J. Phys. B-At. Mol. Opt. Phys.* **56** 025501
[20] Holloway C L, Prajapati N, Artusio-Glimpse A B, Berweger S, Simons M T, Kasahara Y, Alu A and Ziolkowski R W 2022 *Appl. Phys. Lett.* **120** 204001
[21] Song Z, Liu H, Liu X, Zhang W, Zou H, Zhang J and Qu J 2019 *Opt. Express* **27** 8848
[22] Wade C G, Sibalic N, de Melo N R, Kondo J M, Adams C S and Weatherill K J 2017 *Nat. Photonics* **11** 40
[23] Downes L A, MacKellar A R, Whiting D J, Bourgenot C, Adams C S and Weatherill K J 2020 *Phys. Rev. X* **10** 011027
[24] Yuan J, Jin T, Xiao L, Jia S and Wang L 2023 *IEEE Antennas Wirel. Propag. Lett.* **22** 2580
[25] Jiao Y, Han X, Fan J, Raithel G, Zhao J and Jia S 2019 *Appl. Phys. Express* **12** 126002
[26] Li H, Hu J, Bai J, Shi M, Jiao Y, Zhao J and Jia S 2022 *Opt. Express* **30** 13522
[27] Meyer D H, Cox K C, Fatemi F K and Kunz P D 2018 *Appl. Phys. Lett.* **112** 211108
[28] Holloway C L, Simons M T, Haddab A H, Gordon J A, Anderson D A, Raithel G and Voran S D 2021 *IEEE Antennas Propag. Mag.* **63** 63
[29] Anderson D A, Sapiro R E and Raithel G 2021 *IEEE Trans. Antennas Propag.* **69** 2455
[30] Holloway C L, Simons M T, Gordon J A and Novotny D 2019 *IEEE Antennas Wirel. Propag. Lett.* **18** 1853
[31] Cai M, Xu Z, You S and Liu H 2022 *Photonics* **9** 250
[32] Wu F, An Q, Sun Z and Fu Y 2023 *Phys. Rev. A* **107** 043108
[33] Wu B, Yao J, Wu F, An Q and Fu Y 2024 *Chin. Phys. B* **33** 024205
[34] Prajapati N, Rotunno A P, Berweger S, Simons M T, Artusio-Glimpse A B, Voran S D and Holloway C L 2022 *AVS Quantum Sci.* **4** 035001
[35] Yuan J, Jin T, Yan Y, Xiao L, Jia S and Wang L 2024 *EPJ Quantum Technol.* **11** 2
[36] Yang K, Sun Z, Mao R, Lin Y, Liu Y, An Q and Fu Y 2022 *Chin. Opt. Lett.* **20** 081203
[37] Borowka S, Pylypenko U, Mazelanik M and Parniak M 2022 *Appl. Optics* **61** 8806